

Effect of Tensile Deformation on Microstructure and Pitting Resistance of BFS600 Austenitic High-strength Stainless Steel

Yawen Cheng, Yuanyuan Liu*, Guangming Liu, Jiaming Wang, Shengsheng Qian, Jin Li, Yiming Jiang*

Department of Materials Science, Fudan University, Shanghai 200433, People's Republic of China

*E-mail: liuyy@fudan.edu.cn; ymjiang@fudan.edu.cn.

Received: 16 March 2019 / Accepted: 20 May 2019 / Published: 30 June 2019

BFS600 austenitic stainless steel is a newly developed Cr-Mn-Ni-N high-strength stainless steel that aims to be used in the automotive industries. The effects of tensile deformation on the microstructure evolution and pitting behaviors of the BFS600 stainless steels were investigated in this paper. The microstructure and magnetic properties of the tensile-deformed BFS600 stainless steels were evaluated using optical microscopy, x-ray diffraction, scanning electron microscopy, electron backscatter diffraction, the measurement of saturation magnetization and the ferrite meter. It was revealed that the α' -martensite phase had appeared in the steel after the tensile deformation. No ε -martensite phase was identified in this work. The amount of the α' -martensite phase increased as the tensile strain increased. Tensile deformation also resulted in the increase of dislocation density and grain refinement of the BFS600 stainless steel. For the deformed BFS600 austenitic stainless steels, the pitting resistance in NaCl solution decreased first and then increased as the tensile strain increased from 0 to 50%. The worst pitting resistance was present for the sample with a tensile strain of 30%. The dependence of pitting resistance on the tensile strain can be attributed to the combination effects of the increased dislocation density, the transformation of γ phase to α' -martensite phase, and the grain refinement after the tensile deformation.

Keywords: High strength stainless steel, Strain induced martensite, Microstructure characterization, Tensile deformation, Pitting resistance

1. INTRODUCTION

In recent years, there is an increasing focus on the crash safety and fuel economy of automobiles [1, 2]. The service life of the new-energy vehicles, which is closely related to the replaceable battery, has been greatly extended compared to traditional vehicles since battery technology has been greatly developed. Then advanced properties are required for the car-body materials, including long-life, no-coating, high-strength, lightweight and high plasticity [3-8]. The lightweight aluminum and magnesium

alloys, high strength carbon steel, high strength stainless steel and the fiber-reinforced composites are the promising body materials for the new-energy vehicles [9]. Among these potential materials, high-strength carbon steel and the lightweight magnesium/aluminum alloys need protective coatings, and the fiber-reinforced composites are uneconomic to be used as automotive structures in the present [10]. Therefore, considering the combined requirements of high strength, good plasticity, long service life and good corrosion resistance, high-strength stainless steel will be the most promising choice for the new-energy vehicles.

Metastable austenitic stainless steel is a type of high-strength stainless steel with excellent ductility [11]. The replacement of expensive Ni by Mn can reduce the production cost, and the austenite phase is stabilized by the addition of N and Cu atoms. N alloying can also promote the strength of stainless steels [12]. On the other hand, plastic deformation can cause the formation of strain-induced martensite [13-16] in the metastable austenitic stainless steel. Two types of martensite phase may be induced from the austenite phase (γ) after deformation: ϵ -martensite phase and α' -martensite phase. The α' -martensite phase is ferromagnetic with a bcc structure, while the ϵ -martensite phase is paramagnetic with a hcp structure [17]. The strain-induced martensite can significantly improve the strength of the metastable austenitic stainless steel [11].

However, high-density dislocation defects, the strain-induced martensite and the refined grains after deformation make the local corrosion behaviors of the stainless steels more and more complicate. Haanappel and Stroosnijder [18] reported that the pitting potential of 304 stainless steel in NaCl solution decreased after small deformation but increased with the further increased deformation. Guo et al. [19] reported that the pitting corrosion resistance for 2002 duplex stainless steel was insensitive to plastic deformation in both neutral and acid solutions. Alvarez et al. [20] suggested that deformation induced martensite in UNS S3040 and S31603 austenitic stainless steels dissolved at a low potential in an acidic medium. Kamachi et al. [21] revealed that plastic deformation up to 20% enhanced the pitting corrosion resistance of 316L austenitic stainless steel, and thereafter a sudden decrease in pitting corrosion resistance was noticed at higher deformation. Chen and Zhang [22] showed that cold rolling increased the number of pits and decreased the pit size at a certain applied potential for the high-strength low alloy steel. Therefore, a consistent mechanism about the effect of deformation on the pitting resistance of stainless steels has not been clearly established.

BFS600 stainless steel is a Cr-Mn-Ni-N metastable austenitic high-strength stainless steel recently developed by Baosteel Co., Ltd. in China, aiming to be used in the automotive industries [23]. The localized corrosion resistance after deformation strengthening will be the key point in determining whether the BFS600 stainless steel can meet the long-life demand of the new-grade automotive materials (serving for more than 20 years under maintenance-free conditions). Pitting corrosion is one of the most dangerous forms of localized corrosion. Therefore, the aim of this paper is to investigate the pitting behaviors of the Cr-Mn-Ni-N stainless steel after plastic deformation. The microstructure evolution, microhardness, and magnetic properties of the deformed BFS600 stainless steel were investigated using optical microscopy (OM), electron backscattered diffraction (EBSD), x-ray diffraction (XRD), HV hardness measurements, the measurement of saturation magnetization and ferrite meter, respectively. The pitting resistance was studied by the potentiodynamic polarization and critical pitting temperature (CPT) test. The transformation mechanism of the strain-induced martensite during tensile deformation

is discussed. The dependence of corrosion resistance on the tensile deformation is also clarified for the BFS600 stainless steel.

2. EXPERIMENTAL

2.1 Materials and sample preparation

The chemical composition of the Ni-Cr-Mn-N austenitic stainless steel studied in this paper is shown in Table 1.

Table 1. Chemical composition of the BFS600 austenitic high-strength stainless steel (wt%).

Sample	C	Si	P	S	Cr	Ni	N	Mn	Cu	Fe
BFS600	0.06	0.4	0.02	0.002	15.0	1.3	0.16	9.5	1.4	Bal.

Specimens, with a size of 250 mm × 35 mm × 3 mm, were cut from the annealed plates for tensile deformation. Various amounts of deformations ranging from 5%, 10%, 15%, 20%, 30%, 40% to 50% were considered. The tensile-deformed specimens were provided by Baosteel Co., Ltd. For microstructure characterizations and pitting resistance measurement, rectangular samples of 12 mm × 12 mm were cut from the middle parts of these tensile-deformed specimens.

2.2 Characterizations

Phase identification via x-ray diffraction was performed by a D8 ADVANCE x-ray diffractometer (Bruker Corporation, Germany) with a Cu tube operating at 40 kV and 20 mA. The scan was performed from 20° to 100° of 2θ with a step of 0.01°. The α'-martensite phase, ε-martensite phase and γ phase were also identified by the electron backscatter diffraction (EBSD) coupled with a scanning electron microscopy (FEI Quanta 600 FEG) using an accelerating voltage of 15 kV with a scanning step of 1.4 μm. Samples for EBSD characterization were electro-etched in a mixture of 8 vol% perchloric acid and 92 vol% ethanol at an applied voltage of 20.0 V. The microstructure of the deformed steel samples was also observed by optical microscopy (CAIKON 4XCE) after etching in a 10 wt.% oxalic acid solution for 15 seconds at 1 A/cm².

The change of magnetic properties can indirectly signify the amount of α'-martensite phase in the deformed steels [24, 25], therefore, the magnetic properties of the deformed BFS600 stainless steel samples were investigated by a ferrite meter and the saturation magnetization. The volume fraction of the ferromagnetic phase was measured for more than ten different locations on the same specimen surface by a ferrite meter (MP30E-S, Fischer Corporation, Germany). The measurements of saturation magnetization were performed using a vibrating sample magnetometer (Quantum Design, USA). The

micro-hardness for different samples was measured by an HMV-2TADW micro-hardness tester (Shimadzu Corporation, Japan) using a load of 100g.

2.3 Electrochemical tests

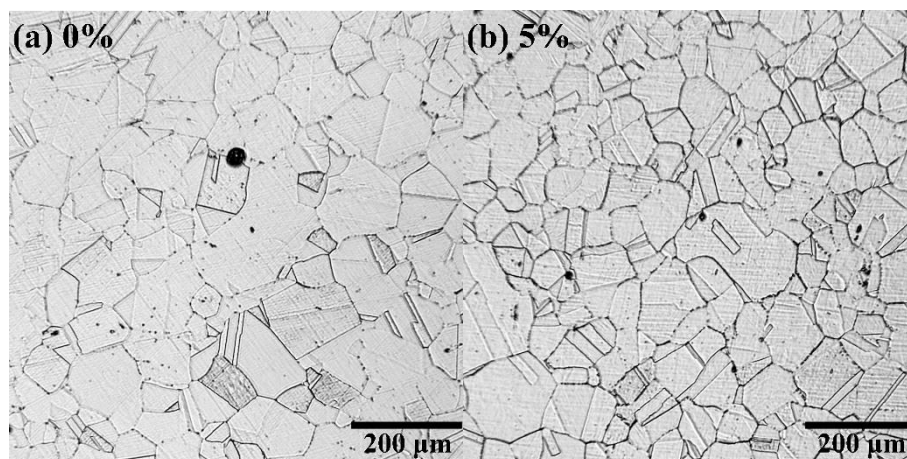
All the samples for the electrochemical tests were mounted in epoxy resin, then mechanically ground with SiC papers from 180 to 2000 grit, and finally polished with a diamond paste of 2.5 μm . To avoid crevice corrosion, the sample surface was covered by 3M tape (3MTM 1600 Vinyl Electrical Tape), leaving an exposed area of 1 cm^2 . All the electrochemical tests were carried out using a CHI660D workstation (Shanghai Chenhua Instrument Co., Ltd, China) with a three-electrode cell. The BFS600 austenitic stainless steel sample served as the working electrode, while a platinum plate and a saturated calomel electrode (SCE) acted as the counter electrode and the reference electrode, respectively.

Potentiodynamic polarization measurements were conducted in a 3.5 wt.% NaCl solution at 25 $^{\circ}\text{C}$ with a scan rate of 0.1667 mV/s. The potential was increased from -400 mV_{SCE} in the anodic direction until the current density reached 1 mA/cm². The applied potential at which the current density reached 100 $\mu\text{A cm}^{-2}$ was defined as the pitting potential (E_{pit}).

The critical pitting temperature (CPT) is another important parameter to evaluate the pitting resistance of stainless steels. CPT test was carried out in a 1 M NaCl solution by applying a constant potential of +200 mV_{SCE} on the BFS600 stainless steel sample and increasing the solution temperature at a constant rate of 1 $^{\circ}\text{C /min}$ from 2 $^{\circ}\text{C}$. In the initial stabilization period, the sample surface was protected by the passive film, and the current density remained stable at a value around 1 $\mu\text{A/cm}^2$. Then the current density increased rapidly as the temperature was further increased. The temperature at which the current density equaled 100 $\mu\text{A/cm}^2$ was defined as the critical pitting temperature.

3. RESULTS AND DISCUSSION

3.1 Microstructure evolution



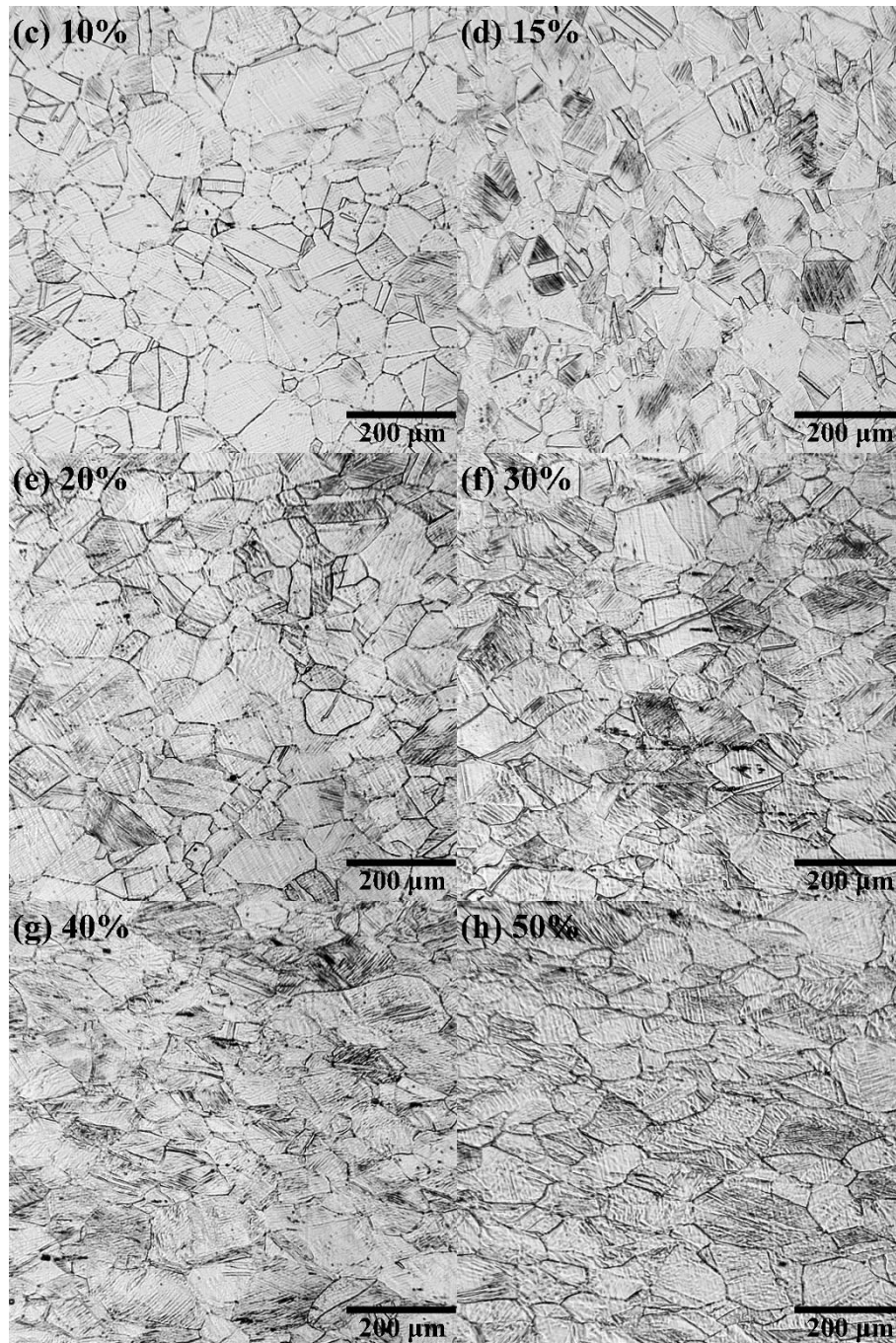


Figure 1. Optical micrographs after etching in 10 wt.% oxalic acid solution for 15 seconds at 1 A/cm^2 for the BFS600 stainless steel samples after different amounts of tensile deformation: (a) 0%, (b) 5%, (c) 10%, (d) 15%, (e) 20%, (f) 30%, (g) 40%, (h) 50%.

Figure 1 shows the optical micrographs of the BFS600 austenitic stainless steel samples with and without tensile deformation after the 10% oxalic acid etching. Step structure of austenitic grains was observed for the BFS600 stainless steel sample before tensile deformation in Figure 1a. Mechanical twins and slip bands showed up on the sample surface after tensile deformation. The number of mechanical twins and slip bands significantly increased as the tensile strain increased from 0 to 20%. Then the change of dislocation density became less obvious with the further increase of tensile strain.

The grains were obviously elongated parallel to the tensile direction for the samples after larger amount of tensile deformation. The size of the austenite grains decreased with the increase of tensile stain, indicating the grain refinement effect of tensile deformation [26]. However, the formation of the martensite phase cannot be distinguished in these optical micrographs.

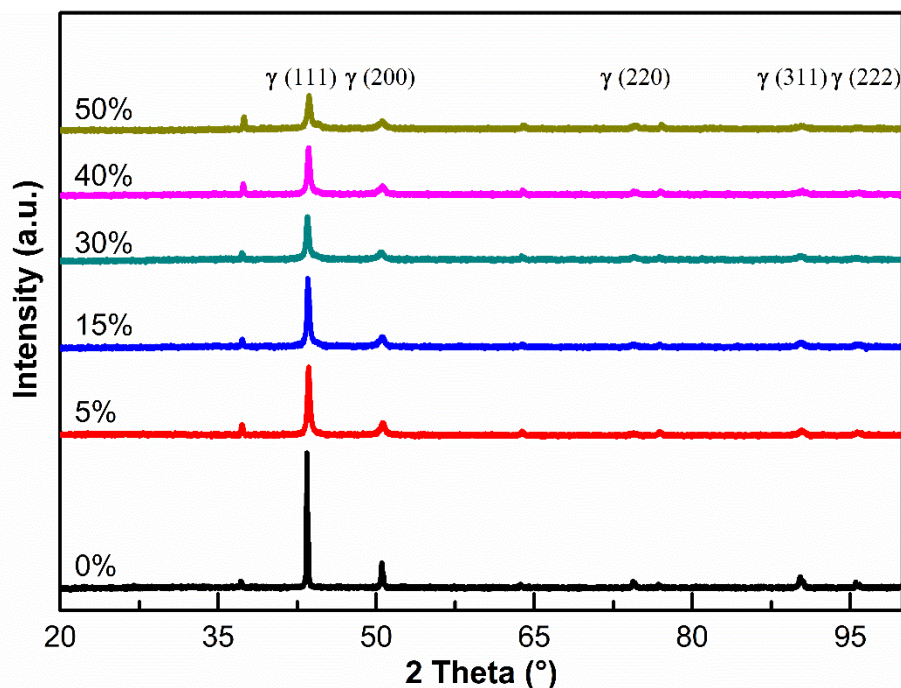


Figure 2. X-ray diffraction spectra for the BFS600 stainless steel samples after different amounts of tensile deformation from 0% to 50%.

In order to identify the phase transformation after tensile deformation, the crystal structure of the BFS600 austenitic stainless steel samples with and without tensile deformation was investigated. As shown in Figure 2, diffraction peaks at the same positions were observed for all the BFS600 austenitic stainless steel samples. The (111), (200), (220), (311) and (222) diffraction peaks were identified for the austenite matrix. The results are consistent with previous studies [19, 24]. Unknown peaks located at around 37.1° , 63.7° and 76.8° of 2θ were observed for all the patterns. These peaks cannot be associated with any possible phase in austenite stainless steel like α' -martensite, ϵ -martensite or ferrite phase, and may originate from the production process. Same diffraction peaks were also observed for the UNS S31803 duplex stainless steel provided by Baosteel Co., Ltd. The intensity of all the diffraction peaks associated with the austenite phase decreased gradually as the amount of tensile deformation increased. This trend is consistent with the microstructure characterization by optical microscopy that the austenite grains were gradually fragmented with the increase of tensile strain. However, no martensite phase can be identified from the XRD results. The content of the strain-induced martensite may be too low to be detectable in the x-ray diffraction, because of the unsatisfied sensitivity and the noise interference in the XRD test.

The EBSD technique is suitable to identify the low-content phases [27], however, its identification ability significantly decreases with the increase of tensile strain. Only the BFS600

austenitic stainless steel samples with 0%, 5% and 15% tensile strains were characterized by the EBSD technique. As can be seen from Figure 3, only the α' -martensite phase with a bcc structure and the austenitic matrix with an fcc structure were identified. No ε -martensite phase was found in the EBSD characterization, suggesting the phase transformation process is from austenite to α' -martensite for the BFS600 austenitic stainless steel during tensile deformation.

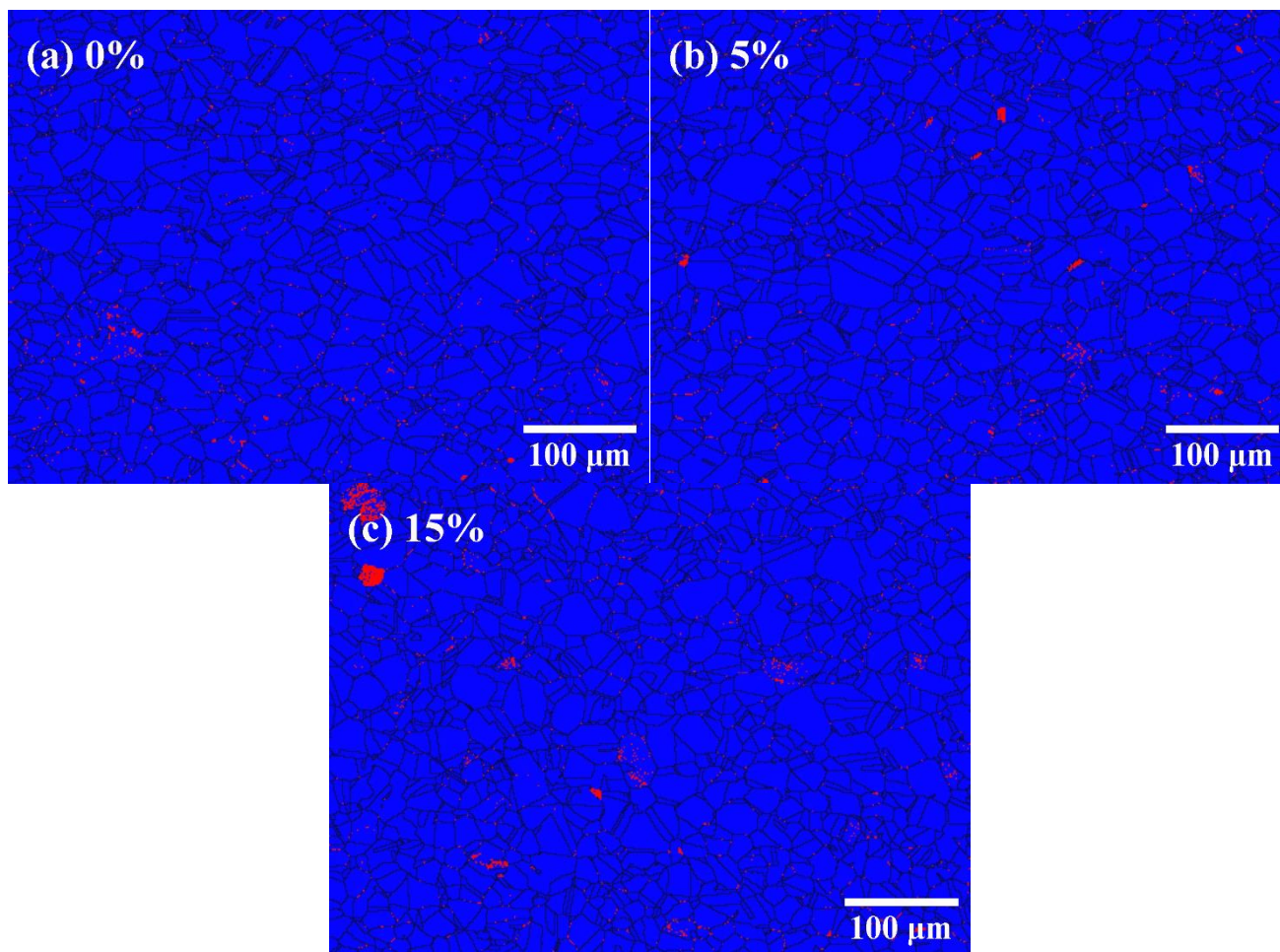


Figure 3. Phase distribution maps for the BFS600 stainless steel samples after different amounts of tensile deformation: (a) 0%, (b) 5%, (c) 15%. Red: the α' martensite phase, blue: the austenite matrix.

The α' -martensite phase mainly located at the austenite grain boundaries. Around 0.60 vol.% α' -martensite phases were revealed for the BFS600 stainless steel sample without the designed tensile deformation. These α' -martensite phases might originate from the thermomechanical processes in production. As the tensile strain increased from 5% to 15%, the volume fraction of the α' -martensite phase increased from 0.72% to 1.14%.

3.2 The α' -martensite content

Since the α' -martensite phase is ferromagnetic and the austenite phase is paramagnetic, the content of the α' -martensite phase can be indirectly measured by the magnetic properties of the BFS600

stainless steel samples [24]. The volume fraction of the α' -martensite phase measured by the ferrite meter is shown in Figure 4 as a function of tensile strain. The volume fraction of the α' -martensite phase changed less as the tensile strain increased from 0% to 5%. This agrees well with the results of EBSD characterization. Then the amount of the α' -martensite phase increased gradually from 0.24% to 5.8% with the increase of tensile strain from 10% to 50%. It is noticed that the content of α' -martensite phase measured by the ferrite meter is lower than the value calculated in the EBSD characterization for the sample with 0%~10% tensile strains. This may result from the fact that the grain boundaries (black in color) had been excluded from the volume-fraction calculation based on the EBSD images, resulting in the smaller amounts of austenite phase and higher volume fraction of the α' -martensite phase.

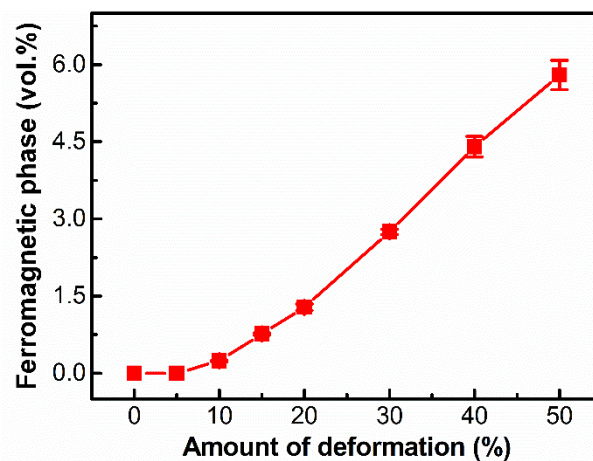


Figure 4. The volume fraction of ferromagnetic phase measured by the ferrite meter for the BSF600 stainless steel samples after different amounts of tensile deformation from 0% to 50%.

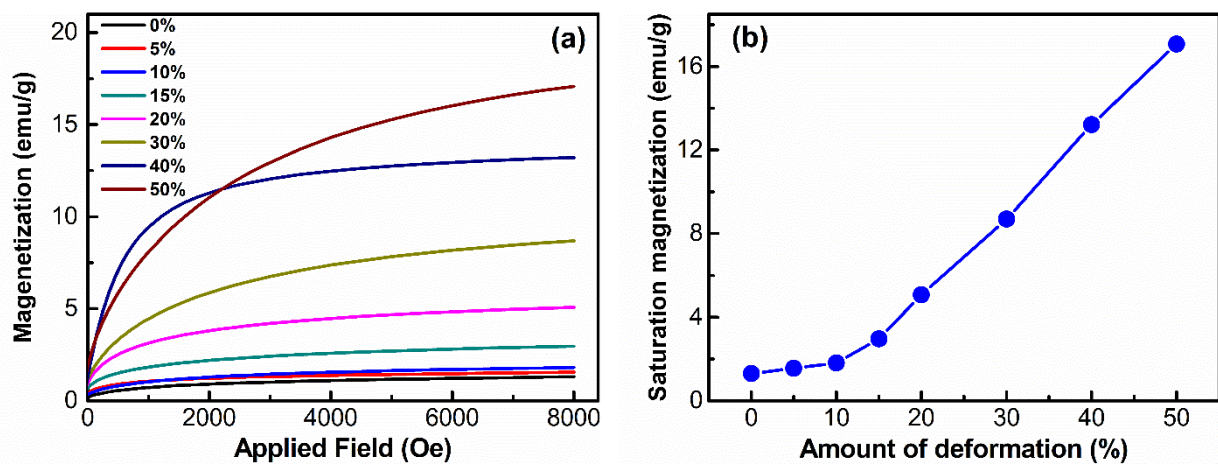


Figure 5. Results of the saturation magnetization measurement for the BSF600 stainless steel samples after different amounts of tensile deformation: (a) Magnetization curves, (b) Saturation magnetization values calculated from the magnetization curves.

To verify the measured results of the ferrite meter, the magnetic properties of the BFS600 austenitic stainless steel samples were also studied by the vibrating sample magnetometer [28, 29]. Figure 5a displays the resulting magnetization curves, and Figure 5b shows the calculated saturation

magnetization values for the samples with different tensile strains. It is obvious that the trend of the saturation magnetization values with tensile strain agrees well with the trend of the volume fraction of ferromagnetic phase shown in Figure 4. The amount of the α' -martensite phase in the BFS600 austenitic stainless steel sample increased with the increasing of tensile strain. The increase rate is small for the strains of no more than 10%, while a much larger increase rate is present for the strains higher than 10%.

3.3 Microhardness

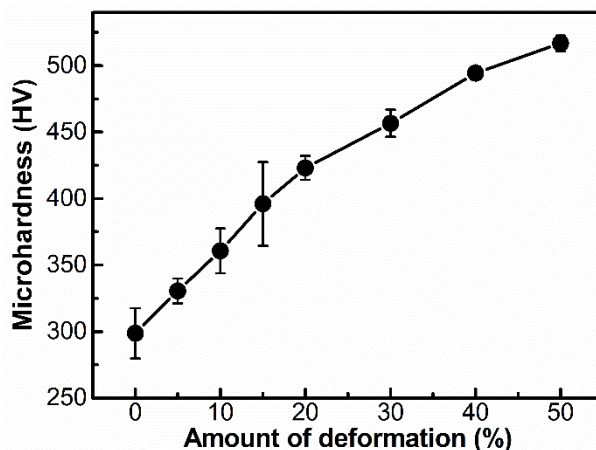


Figure 6. The HV hardness for the BFS600 stainless steel samples after different amounts of tensile deformation from 0% to 50% measured with a load of 100g.

The microhardness of the BFS600 austenitic stainless steel samples is given in Figure 6. The microhardness increased from 298.6 HV to 516.8 HV as the tensile deformation changed from 0% to 50%. The increase of dislocation density and the formation of strain-induced α' -martensite can both contribute to this increase of microhardness [19, 30]. However, it is worth noting that the increase rate of microhardness declined when the tensile strain exceeded 20%, which is different from the increase trend of the α' -martensite phase. It is known from the optical images in Figure 1 that the dislocation density has significantly increased with the increased tensile strain up to 20%. This indicates that the strain-dependent dislocation density contributes more to the hardness evolution than the formation of the α' -martensite phase [30].

3.4 Pitting resistance

Figure 7 shows the potentiodynamic polarization curves for the BFS600 stainless steel samples after different tensile deformations in a 3.5 wt.% NaCl solution at 25 °C. All the polarization curves have similar shape, and not much difference can be observed for the cathodic branch. However, much more metastable current peaks were present in the polarization plots for the samples after tensile deformation. The calculated electrochemical parameters are listed in Table 2 except the pitting potential. The pitting potential (E_{pit}) value, which is a frequently used parameter to evaluate the pitting resistance of stainless steel [31, 32], is summarized in Figure 8 as a function of tensile deformation. As the tensile strain

increased from 0% to 30%, the E_{pit} value of the BFS600 stainless steel samples decreased gradually from 233 mV_{SCE} to 127 mV_{SCE}. Then the E_{pit} value increased to 207 mV_{SCE} as the tensile deformation further increased from 30% to 50%, however, the E_{pit} value of the 50%-deformed sample was still lower than that of the sample without deformation. This dependence of pitting potential on the degree of deformation is consistent with the results of the deformed 304 stainless steel in NaCl solution [18].

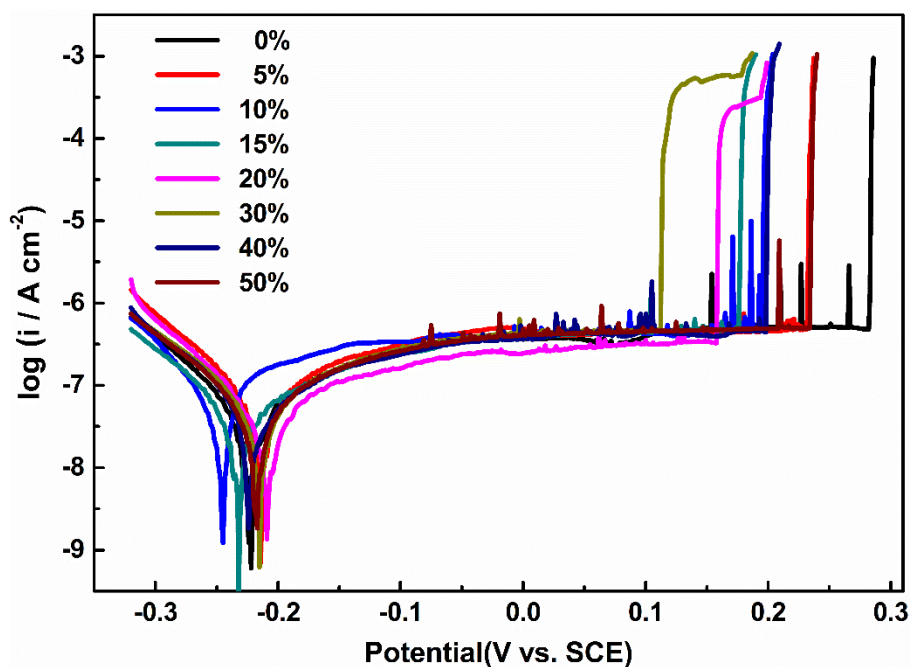


Figure 7. Potentiodynamic polarization curves in the 3.5 wt.% NaCl solution at 25 °C for the BSF600 stainless steel samples after different amounts of tensile deformation from 0% to 50%.

Table 2. Corrosion parameters derived from the polarization curves in 3.5 wt.% NaCl solution for BSF600 stainless steel samples after different amounts of tensile deformation. The corrosion potential, corrosion current density and passive current density are marked as E_{corr} , i_{corr} and i_{p} , respectively.

Sample with different tensile deformations	$E_{\text{corr}}/\text{mV}_{\text{SCE}}$	$\log(i_{\text{corr}}/\text{A}\cdot\text{cm}^{-2})$	$\log(i_{\text{p}}/\text{A}\cdot\text{cm}^{-2})$
0	-234	-7.25	-6.29
5%	-234	-7.04	-6.36
10%	-247	-7.01	-6.34
15%	-241	-7.32	-6.37
20%	-224	-7.20	-6.47
30%	-230	-7.15	-6.34
40%	-240	-7.24	-6.39
50%	-230	-7.19	-6.35

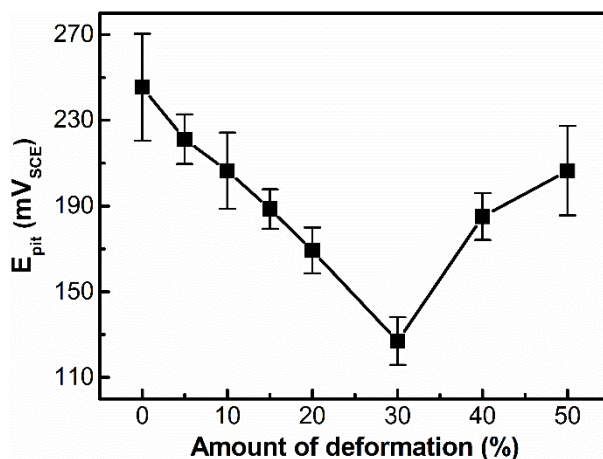


Figure 8. Pitting potential derived from the polarization curves for the BSF600 stainless steel samples after different amounts of tensile deformation in the 3.5 wt.% NaCl solution

Figure 9 illustrates the current density curves for the BFS600 stainless steel samples after different tensile deformations in the critical pitting temperature test with an applied potential of 250 mV_{SCE} and at 1 mol/L NaCl solution. The un-deformed samples have the best pitting performance in the CPT test. Much more metastable current transients and much lower breakdown temperatures were observed for the samples after tensile deformation. The derived CPT values are shown in Figure 10 as a function of tensile strain. The CPT value of the un-deformed sample was 21.5 °C, which was significantly higher than the CPT values of the other samples. The dependence of the CPT value on the tensile deformation is similar to the trend of the E_{pit} value. The CPT value also decreased first and then increased with the increased tensile strain from 0% to 50%. The sample with a 30% tensile strain presented the lowest CPT value of 13.5 °C.

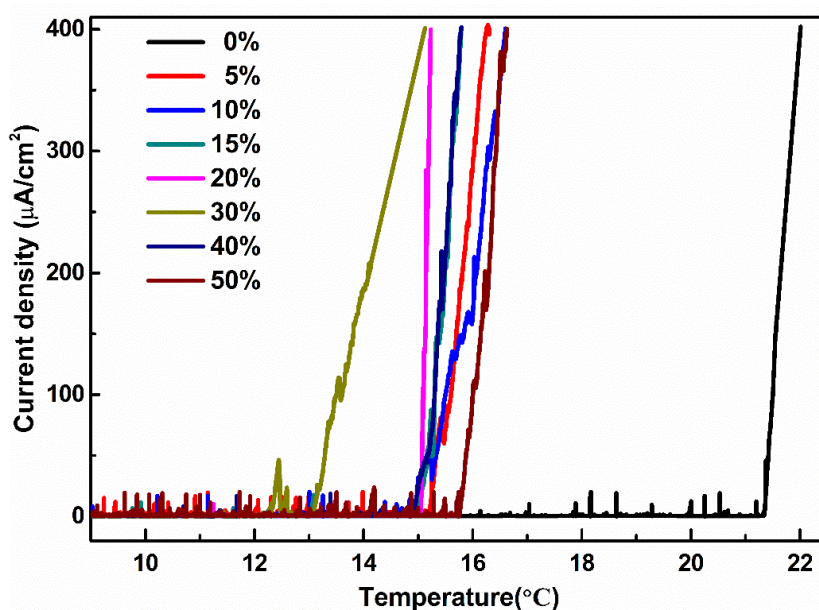


Figure 9. The current density curves in the critical pitting temperature test with a 1 M NaCl solution and an applied potential of 200 mV_{SCE} for the BSF600 stainless steel samples after different amounts of tensile deformation

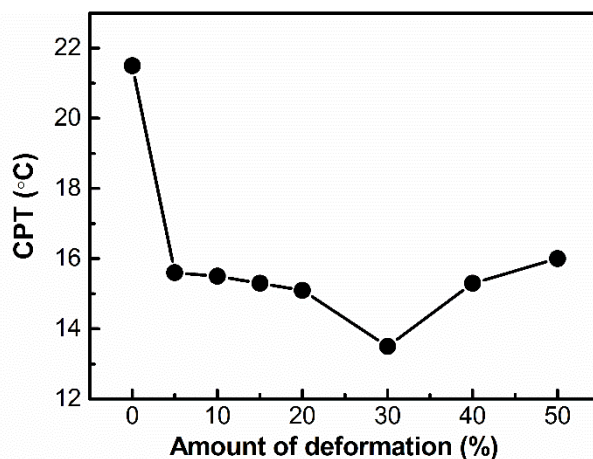


Figure 10. The derived critical pitting temperature values for the BSF600 stainless steel samples after different amounts of tensile deformation in 1M NaCl solution.

It is also reported that the pit initiation frequency of AISI 304 and AISI 430 stainless steels showed a maximum after 10% tensile deformation or 20% cold-rolling reduction [33]. The dislocation pile-ups can stand as active sites and are preferentially dissolved in the corrosion medium, resulting in that the dislocation pile-ups, rather than the strain-induced martensite, governs the sensitivity to corrosion of the deformed stainless steel. On the other hand, grain refinement can promote the pitting resistance of materials [22, 34], and a stable, thicker and compact passive film was found after grain refinement [35]. In the present work, the dislocation density and the content of α' -martensite phase both increased as the tensile strain increased from 0% to 30%. This can account for the deteriorated pitting resistance as the tensile strain increased from 0% to 30%. With the further increase of tensile strain from 30% to 50%, the increase rate of dislocation density declined, making grain refinement the dominant factor that promotes the pitting resistance of the deformed samples.

4. CONCLUSIONS

In this paper, the effects of tensile deformation on the microstructure evolution and pitting resistance were studied for the BFS600 austenitic high-strength stainless steel. The following conclusions can be drawn:

1. The kind of martensite formed in the BFS600 stainless steel during tensile deformation was the α' -martensite phase. With the increase of the tensile strain, the dislocation density, the amount of the strain-induced α' -martensite phase and the microhardness all increased. The increase of dislocation density contributed more to the increase of microhardness than the strain-induced α' -martensite phase.

2. In the neutral NaCl solutions, the pitting potential and the critical pitting temperature values of the deformed BFS600 stainless steel samples both decreased first, and then increased with the increase of tensile strain. The worst pitting resistance was present for the sample with a tensile strain of 30%.

3. The deteriorated pitting resistance associated with the smaller deformations can be attributed to the increase of dislocation density and the formation of the α' -martensite phase, while the further promoted pitting resistance with the further increased tensile strain can be ascribed to the effect of grain refinement.

ACKNOWLEDGEMENTS

This work was financially supported by the National Key Research and Development Program of China (No. 2018YFB0704400) and the National Natural Science Foundation of China (No. 51801028, No. 51871061 and No. 51671059). The authors also gratefully acknowledge the helpful collaboration, technical assistance and the original samples provided by Dr. Hongyun Bi and Haigang Xu from Baosteel Co., Ltd.

References

1. Y.H. Kim, K.Y. Kim and Y.D. Lee, *Mater. Manuf. Process*, 19 (2004) 51.
2. M. Eskandari, A. Najafizadeh and A. Kermanpur, *Mater. Design*, 30 (2009) 3869.
3. Y. Hu, S. Yurkovich, Y. Guezennec and B.J. Yurkovich, *J. Power Sources*, 196 (2011) 449.
4. G. Davies, *Materials for Automobile Bodies*, Butterworth-Heinemann, (2003) Oxford, England.
5. M. Tisza and I. Czinege, *International Journal of Lightweight Materials and Manufacture*, 1 (2018) 229.
6. X. Cui, H. Zhang, S. Wang and J. Ko, *Mater. Design*, 32 (2011) 815.
7. A.M. Sherman and K.H.J. Buschow, *Encyclopedia of Materials: Science and Technology*, Elsevier, (2001) Oxford, England.
8. A. Patil, A. Patel and R. Purohit, *Mater. Today*, 4 (2017) 3807.
9. M. Kiani, I. Gandikota, M. Rais-Rohani and K. Motoyama, *J. Magnes. Alloy*, 2 (2014) 99.
10. V. Dhand, G. Mittal, K.Y. Rhee, S.J. Park and D. Hui, *Compos. Part. B-Eng.*, 73 (2015) 166.
11. M. Smaga, F. Walther and D. Eifler, *Mat. Sci. Eng. A-Struct.*, 483-484 (2008) 394.
12. J. Liu, G. Fan, P. Han, J. Liu and J. Gao, *Mat. Sci. Forum*, 620-622 (2009) 161.
13. A. Weisbrodt-Reisch, M. Brummer and B. Hadler, *Mat. Sci. Eng. A-Struct.*, 416 (2006) 1.
14. M. Murayama, K. Hono and Y. Katayama, *Mater. Sci. Tech.-Lond.*, 30 (1991) 137.
15. G.B. Olson and M. Cohen, *Metall. Trans. A*, 6 (1975) 791.
16. L.E. Murr, K.P. Staudhammer and S.S. Hecker, *Metall. Trans.*, 13 (1982) 627.
17. M. Humbert, B. Petit and B. Bolle, *Mat. Sci. Eng. A-Struct.*, 454-455 (2007) 508.
18. V. Haanappel and M.F. Stroosnijder, *Corrosion*, 57 (2001) 557.
19. Y. Guo, J. Hu, Y. Jiang and J. Li, *Int. J. Electrochem. Sci.*, 11 (2016) 4812.
20. S.M. Alvarez, A. Bautista and F. Velasco, *Corros. Sci.*, 69 (2013) 130.
21. U. Kamachi Mudail, P. Shankar and S. Ningshen, *Corros. Sci.*, 44 (2002) 2183.
22. Y. Chen and K. Zhang, *Adv. Mater. Res.*, 557-559 (2012) 143.
23. H. Bi, E. Chang and L. Xin, *Baosteel Technical Research*, 11 (2017) 34.
24. X. Si, J. Wu, Y. Tang, J. Li and Y. Jiang, *Int. J. Electrochem. Sci.*, 12 (2017) 3916.
25. T. Fukuda, T. Kakeshita and K. Kindo, *Mat. Sci. Eng. A-Struct.*, 438-440 (2006) 212.
26. M. Orłowska, E. Ura-Bińczyk and L. Olejnik, *Corros. Sci.*, 148 (2019) 57.
27. Y. Zhang, M. Li and H. Bi, *Mat. Sci. Eng. A-Struct.*, 724 (2018) 411.
28. J. Diang, H. Hung, P.G. McCormick, and R. Street, *J. Magn. Magn. Mater.*, 139 (1995) 109.
29. T. Jayakumar, T.D. Koble, W.A. Theiner, and Baldev Raj, *Nondestruct. Test. Eva.*, 10 (1993) 205.
30. M. Shirdel, H. Mirzadeh and M.H. Parsa, *Mater. Charact.*, 103 (2015) 150.
31. P. Marcus, V. Maurice and H.H. Strehblow, *Corros. Sci.*, 50 (2008) 2698.

32. A. Pardo, M.C. Merino, A.E. Coy, F. Viejo, R. Arrabal and E. Matykina, *Corros. Sci.*, 50 (2008) 1796.
33. L. Peguet, B. Malki and B. Baroux, *Corros. Sci.*, 49 (2007) 1933.
34. A.D. Schino and J.M. Kenny, *J. Mater. Sci. Lett.*, 327 (2002) 1969.
35. A. Fattah-alhosseini and S. Vafaeian, *J. Alloy. Compd.*, 639 (2015) 301.

© 2019 The Authors. Published by ESG (www.electrochemsci.org). This article is an open access article distributed under the terms and conditions of the Creative Commons Attribution license (<http://creativecommons.org/licenses/by/4.0/>).